

CrossMark  
click for updatesCite this: *J. Mater. Chem. C*, 2016,  
4, 315Ultrathin nanosheets of CrSiTe<sub>3</sub>: a semiconducting  
two-dimensional ferromagnetic material†Ming-Wei Lin,<sup>‡a</sup> Houlong L. Zhuang,<sup>‡a</sup> Jiaqiang Yan,<sup>bc</sup> Thomas Zac Ward,<sup>c</sup>  
Alexander A. Puretzky,<sup>a</sup> Christopher M. Rouleau,<sup>a</sup> Zheng Gai,<sup>a</sup> Liangbo Liang,<sup>ad</sup>  
Vincent Meunier,<sup>d</sup> Bobby G. Sumpter,<sup>ae</sup> Panchapakesan Ganesh,<sup>a</sup> Paul R. C. Kent,<sup>ae</sup>  
David B. Geohegan,<sup>a</sup> David G. Mandrus<sup>bc</sup> and Kai Xiao<sup>\*a</sup>

Finite range ferromagnetism and antiferromagnetism in two-dimensional (2D) systems within an isotropic Heisenberg model at non-zero temperature were originally proposed to be impossible. However, recent theoretical studies using an Ising model have shown that 2D magnetic crystals can exhibit magnetism. Experimental verification of existing 2D magnetic crystals in this system has remained exploratory. In this work we exfoliated CrSiTe<sub>3</sub>, a bulk ferromagnetic semiconductor, to mono- and few-layer 2D crystals onto a Si/SiO<sub>2</sub> substrate. Raman spectra indicate good stability and high quality of the exfoliated flakes, consistent with the computed phonon spectra of 2D CrSiTe<sub>3</sub>, giving strong evidence for the existence of 2D CrSiTe<sub>3</sub> crystals. When the thickness of the CrSiTe<sub>3</sub> crystals is reduced to a few layers, we observed a clear change in resistivity at 80–120 K, consistent with theoretical calculations of the Curie temperature ( $T_c$ ) of ~80 K for the magnetic ordering of 2D CrSiTe<sub>3</sub> crystals. The ferromagnetic mono- and few-layer 2D CrSiTe<sub>3</sub> indicated here should enable numerous applications in nano-spintronics.

Received 22nd October 2015,  
Accepted 25th November 2015

DOI: 10.1039/c5tc03463a

www.rsc.org/MaterialsC

## Introduction

The emergence of novel properties and potential applications of two-dimensional (2D) crystals has recently stimulated considerable worldwide attention.<sup>1–3</sup> A particularly interesting class of candidate 2D crystals are the layered magnetic semiconductors which can simultaneously display semiconductor characteristics and magnetic ordering that are advantageous for optoelectronics and nano-spintronics applications.<sup>4–6</sup> Both ferromagnetic (FM) and antiferromagnetic (AFM) layered semiconductors have been

characterized in bulk form, including their crystallographic and magnetic structures.<sup>7–11</sup> For example, chromium tellurosilicate (CrSiTe<sub>3</sub>) is a FM layered transition-metal chalcogenide (TMD) semiconductor, and exhibits ferromagnetic ordering at 32 K in the bulk.<sup>7–8</sup> Heisenberg type ferromagnetism has been found below 6.25 K for K<sub>2</sub>CuF<sub>4</sub> bulk crystals due to one percent of the anisotropic interlayer exchange interaction.<sup>11</sup> Unlike other non-magnetic 2D layered materials that require edge,<sup>12,13</sup> strain engineering,<sup>14,15</sup> a balanced hole-electron “resonance” condition,<sup>16</sup> or so called phase incorporation due to vacancies<sup>17</sup> to achieve magnetic properties, the magnetic ordering in these 2D systems, such as CrSiTe<sub>3</sub> or K<sub>2</sub>CuF<sub>4</sub>, could inherit magnetic properties from their parent layered 3D system. However, the existence of 2D magnetic ordering is unclear, particularly whether this is inherited from the parent 3D system. In an earlier report, calculations by Mermin and Wagner predicted that spontaneous ferromagnetism and anti-ferromagnetism should not exist based on a 2D isotropic Heisenberg model with long-range order at non-zero temperature.<sup>18</sup> Bruno also proved the absence of spontaneous magnetic ordering in one- or two-dimensional Heisenberg systems with long-range interactions at finite temperatures.<sup>19</sup> Recently, the possibility of 2D K<sub>2</sub>CuF<sub>4</sub> crystals forming free-standing 2D flakes by exfoliation with a robust magnetic moment of a Kosterlitz–Thouless type system was predicted from a first-principles theoretical analysis.<sup>5</sup> Experimentally, a 2D Mn stearate (MnSt<sub>2</sub>) magnet has been demonstrated by deposition on a Si substrate using Langmuir–Blodgett technique.<sup>20</sup>

<sup>a</sup> Center for Nanophase Materials Sciences, Oak Ridge National Laboratory, Oak Ridge, TN 37831, USA. E-mail: xiaok@ornl.gov<sup>b</sup> Department of Materials Science and Engineering, University of Tennessee, Knoxville, TN 37996, USA<sup>c</sup> Materials Science and Technology Division, Oak Ridge National Laboratory, Oak Ridge, TN 37831, USA<sup>d</sup> Department of Physics, Applied Physics, and Astronomy, Rensselaer Polytechnic Institute, Troy, New York 12180, USA<sup>e</sup> Computer Science and Mathematics Division, Oak Ridge National Laboratory, Oak Ridge, TN 37831, USA† Electronic supplementary information (ESI) available: Results of theoretical calculations using various  $U_{\text{eff}}$  ranging from 0 to 10 eV are given in the Fig. S1. Detail information of Raman calculations for both monolayer and bulk is shown in the Fig. S2. Resistivity versus temperature measurements for the thickness of 8.5 nm, 20 nm, 36 nm and 125 nm are demonstrated in the Fig. S3. Fig. S4 illustrates the energies computed from different AFM spin textures, with p-type doping consideration. See DOI: 10.1039/c5tc03463a

‡ These authors contributed equally to this work.

Moreover, a magnetic phase transition exhibiting a thickness dependence due to a dramatic critical exponent  $\beta$  change has been reported for Ni thin film,<sup>21,22</sup> indicating changes in magnetic ordering for a 2D Ising system at non-zero temperature. Recent studies associated with TMDs (TiCoO, CoSe and ZnO) nanosheets using chemical solution approaches also showed the semiconductor characteristics with magnetism,<sup>23–26</sup> demonstrating the existence of magnetism for 2D nanosheets at non-zero temperatures. To resolve the debate on the presence and origin of magnetism in these systems, layered 2D semiconductors, such as CrSiTe<sub>3</sub>, can be exfoliated layer-by-layer from a bulk crystal and can be used as excellent testbeds.

CrSiTe<sub>3</sub> is an indirect layered semiconductor with indirect and direct band gaps at 0.4 eV and 1.2 eV, respectively.<sup>8</sup> As shown in Fig. 1, CrSiTe<sub>3</sub> is a layered material formed from stacks of Te–(Cr, Si)–Te sandwich layers. One layer is composed of a Si<sub>2</sub>Te<sub>6</sub> with two Cr ions inserted between two layers of Te planes, leading to a van der Waals gap.<sup>27</sup> Bulk CrSiTe<sub>3</sub> exhibits a quasi-2D Ising ferromagnetic behavior at  $T_c = 33$  K<sup>28,29</sup> Our previous report shows the strong coupling between the magnetic and lattice degrees of freedom by the phonon measurements across the 33 K ferromagnetic transition.<sup>8</sup> The Si–Te stretching and Te displacement modes are sensitive to the magnetic ordering transition,<sup>8</sup> which indicates the magnetic ordering transition could be modified by a phonon dimensionality crossover in 2D systems due to the quantum confinement of phonons. Recently, based on a Heisenberg model, it was predicted that 2D ferromagnetic CrSiTe<sub>3</sub> was dynamically stable and that the Curie temperature ( $T_c$ ) would be dramatically shifted to higher temperature in single layer compared to the bulk.<sup>30,31</sup> In some published results, they also showed the existence of uniaxial easy axis for monolayer CrSiTe<sub>3</sub> crystal based on 2D Ising model, which was more suitable to predict the  $T_c$  change.<sup>5,32</sup> However, other theoretical calculations predicted that monolayer CrSiTe<sub>3</sub> should be antiferromagnetic with a zigzag spin texture when the significance of second and third order exchange interactions are considered.<sup>6</sup> Although theoretical

studies have predicted the existence of such a 2D magnetic semiconductor, experimental confirmation is still lacking. Unlike graphene or binary semiconductors such as MoSe<sub>2</sub> and GaSe, which have been synthesized using chemical vapor deposition (CVD) and vapor phase deposition (VPD),<sup>33,34</sup> monolayer and few-layer 2D CrSiTe<sub>3</sub> crystals are much harder to synthesize. Recent advances in micro-exfoliation techniques have made it possible to produce 2D magnetic single crystals that were previously inaccessible to the community.<sup>35,36</sup>

In this work, single-crystalline monolayer and few-layer CrSiTe<sub>3</sub> crystals were prepared from bulk crystals by a simple mechanical exfoliation method. The Raman spectra indicate good stability and high quality of the exfoliated flakes, consistent with the computed phonon spectra of 2D CrSiTe<sub>3</sub>, giving a strong evidence for the existence of 2D CrSiTe<sub>3</sub> crystals. When the thickness of the CrSiTe<sub>3</sub> crystals is reduced to few-layers, we observed a clear change in resistivity at 80–120 K, which strongly supports the theoretically predicted temperature enhancement of magnetic ordering ( $T_c \sim 80$  K) for 2D CrSiTe<sub>3</sub> crystals. This study, indicating a combination of semiconducting and magnetic characteristics of 2D CrSiTe<sub>3</sub>, appears promising for a new class of 2D materials for nano-spintronic applications.

## Experimental and theoretical methods

CrSiTe<sub>3</sub> flakes were first deposited by a mechanical cleavage method onto 290 nm-thick, heavily doped Si/SiO<sub>2</sub> substrates. Sample thicknesses were characterized by both a Nikon LV150 optical microscope (OM) and an atomic force microscope (AFM) (Bruker Dimension Icon). MicroRaman spectroscopy (Renishaw, 532 nm excitation with a 50 $\times$  objective) was performed to characterize the typical Raman modes of CrSiTe<sub>3</sub> flakes for different thickness. CrSiTe<sub>3</sub> FET devices were fabricated using standard e-beam lithography (FEI Nanolab 600 dual beam), followed by metal deposition using an e-beam evaporator with a layer of 5 nm Ti and 30 nm Au for both source and drain electrodes. The electrical properties of the devices were then measured in a cryogenic vacuum chamber (Desert Cryogenics,  $\sim 10^{-6}$  torr) with a Keithley 4200 semiconductor analyzer in a back-gating configuration.

Electronic structure calculations of monolayer CrSiTe<sub>3</sub> were carried out using the projector augmented wave (PAW) method within density functional theory (DFT) as implemented in the plane wave code VASP.<sup>37,38</sup> The cutoff energy of the plane-wave basis was set to 700 eV. To represent the localized Cr *d* orbitals, the local density functional approximation (LDA) combined with an on-site Hubbard  $U$  were employed.<sup>39</sup> In the main text, results obtained using  $U_{\text{eff}} = 3.5$  eV are primarily reported. This  $U_{\text{eff}}$  parameter has been shown to reproduce reasonable spin-up/down bandgaps of bulk CrSiTe<sub>3</sub>. Results using various  $U_{\text{eff}}$  ranging from 0 to 10 eV are given in the ESI,<sup>†</sup> Fig. S1. The Monkhorst–Pack scheme was used for  $k$ -point sampling employing a  $9 \times 9 \times 1$   $\Gamma$ -centered grid.

Calculations were also performed to predict the non-resonant Raman scattering spectra of CrSiTe<sub>3</sub> using fully relaxed geometries.

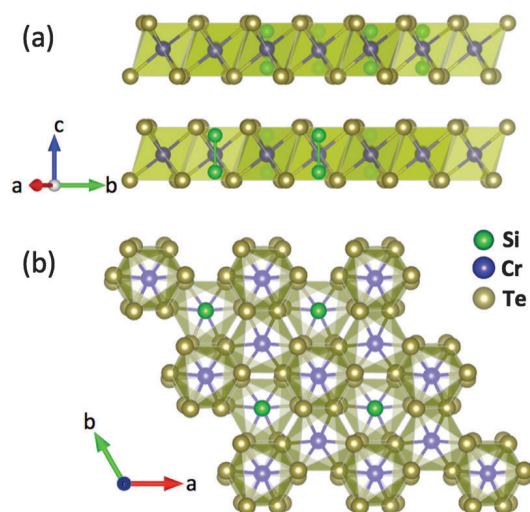


Fig. 1 Side (a) and top (b) views of the atomic structure for 2D CrSiTe<sub>3</sub>.

Since the Raman scattering intensity  $I$  is proportional to  $|e_i \cdot \tilde{R} \cdot e_s|^2$ , the calculations of the Raman tensors  $\tilde{R}$  are most important. This requires information on the phonon frequencies, phonon eigenvectors and the changes of the dielectric constant tensors by phonon vibrations.<sup>40</sup> To calculate Raman scattering intensities, calculation of the dynamic matrix and derivatives of the dielectric constant tensors are required. The dynamic matrix was obtained using the *ab initio* direct method<sup>41</sup> as implemented in the PHONON software.<sup>42</sup> In this finite difference scheme, the Hellmann–Feynman forces in the supercell were computed using VASP for both positive and negative atomic displacements ( $\delta = 0.03 \text{ \AA}$ ) and used in PHONON<sup>42</sup> to construct the dynamic matrix. Diagonalization of the dynamic matrix provides phonon frequencies and eigenvectors. For both positive and negative atomic displacements ( $\delta = 0.03 \text{ \AA}$ ) in the single unit cell, the dielectric tensors were computed by VASP using density functional perturbation theory and then imported into PHONON to generate their derivatives. From this, the Raman intensity for every phonon mode was obtained for a given laser polarization and wavelength to yield a Raman spectrum after Gaussian broadening.

## Results and discussion

CrSiTe<sub>3</sub> single crystals were grown using a self-flux technique as shown in our previous work.<sup>8</sup> The as-grown crystals are plate-like with a thickness around 5 mm. The crystals exhibited very high purity and excellent crystallinity. The van der Waals interaction in the layered CrSiTe<sub>3</sub> single crystals allows it to

be thinned down to atomically thin 2D crystals using mechanical exfoliation. The cleavage energy of CrSiTe<sub>3</sub> (43.7 meV per atom) computed from DFT calculations is significantly smaller than that of MoS<sub>2</sub> (77 meV per atom). Thus, CrSiTe<sub>3</sub> layers of  $\sim 3\text{--}5 \text{ nm}$  in thickness can be easily produced from exfoliation using adhesive tape, and even flakes as thin as only single layer (0.8 nm) are accessible, as illustrated by the image of a large ( $> 5 \mu\text{m}$ ) single layer flake in Fig. 2. Fig. 2(c) and (d) show thicknesses of 0.8 nm and 3 nm (insets shown the line profiles) corresponding to exposed regions of mono- and four-layer flakes, respectively. These results establish that a monolayer of CST on Si/SiO<sub>2</sub> substrate can be made.

The quality and stability of the atomically thin CrSiTe<sub>3</sub> single crystal flakes were further characterized by Raman spectroscopy and calculations of the phonon spectrum for monolayer of CrSiTe<sub>3</sub> crystals. Fig. 3(a) shows the Raman spectrum of CrSiTe<sub>3</sub> flakes with various thicknesses ranging from monolayer to bulk. We observed three peaks located at  $101 \text{ cm}^{-1}$ ,  $125 \text{ cm}^{-1}$  and  $142 \text{ cm}^{-1}$ , which can be assigned to  $E_g$  and  $A_g^2$  and  $A_g^1$  modes, respectively. According to our calculations these modes correspond to in-plane and out-of-plane vibrations of Te atoms (see Fig. 3(b)). The detailed simulation results for the Raman active modes in a CrSiTe<sub>3</sub> crystal are shown in Fig. S2 (ESI<sup>†</sup>). The calculated frequencies agree well with the measured positions of the Raman peaks. In addition, all phonon frequencies observed in the first Brillouin zone are real, confirming the dynamic stability of a single CrSiTe<sub>3</sub> layer. The observed peaks show blue shift of a few wavenumbers as the number of layers decreases that can be related to variations of the phonon spectra due to the reduced dimensionality.<sup>34</sup> We also observed a dramatic

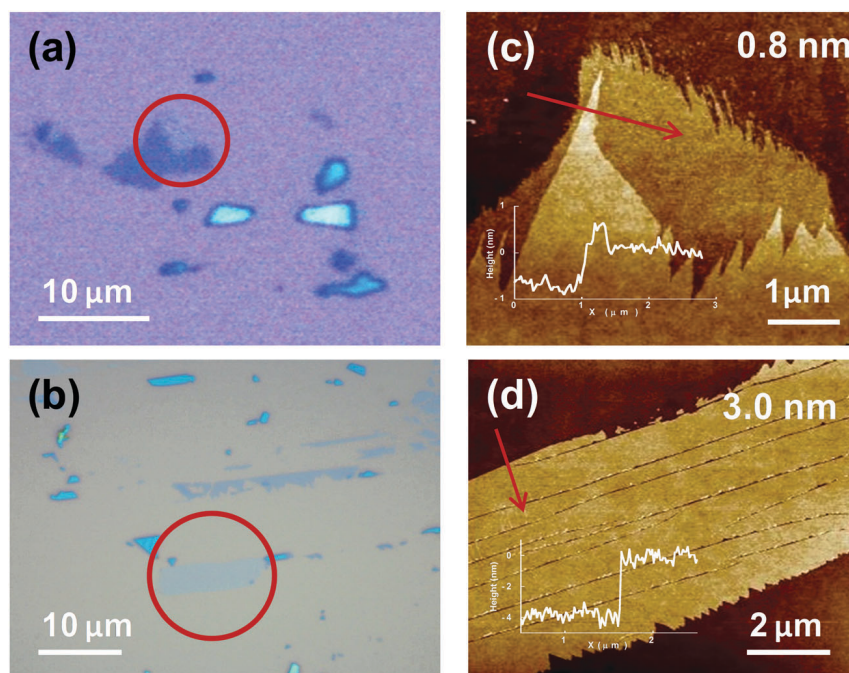


Fig. 2 The optical and AFM images of exfoliated 2D CrSiTe<sub>3</sub> flakes on Si/SiO<sub>2</sub> substrates. (a and b) Optical images showing CrSiTe<sub>3</sub> flakes by exfoliation method on Si/SiO<sub>2</sub> substrate with mono and few layers. (c and d) AFM images demonstrating the mono and few-layer CrSiTe<sub>3</sub> flakes with respect to (a) and (b). Insets in (c) and (d) are line scan profiles of red arrows.

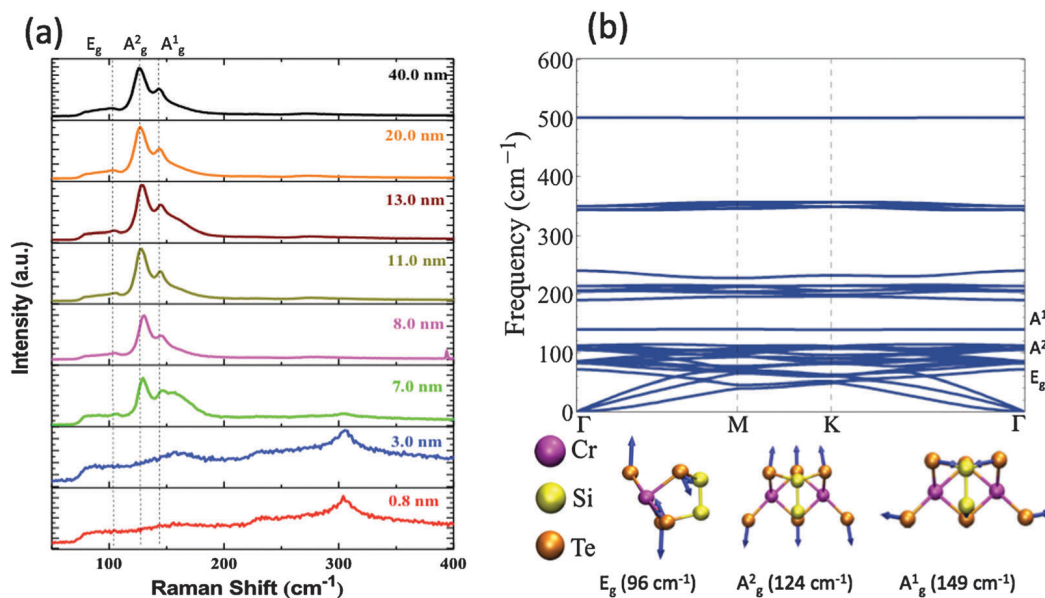


Fig. 3 Measured Raman and phonon dispersion spectrum from first principles simulations for CrSiTe<sub>3</sub> flakes. (a) Illustrates Raman spectrum of CrSiTe<sub>3</sub> flakes with different thickness, showing the typical peaks at 142 cm<sup>-1</sup>, 125 cm<sup>-1</sup> and 101 cm<sup>-1</sup>. The broad peak at 304 cm<sup>-1</sup> belongs to Si. (b) The phonon spectrum demonstrates the dynamic stability for mono-layer CrSiTe<sub>3</sub>. The active Raman modes from simulation corresponding to A<sub>g</sub><sup>1</sup> (in-plane), A<sub>g</sub><sup>2</sup> (out-of-plane) and E<sub>g</sub> (out-of-plane) of Te vibrations match the Raman peaks obtained from measurements.

change in the Raman spectra when the thickness decreased from 7 nm to 3 nm, *i.e.*, all three sharp peaks disappear and only a broad feature at  $\sim 160$  cm<sup>-1</sup> still remains in the spectra, but with much lower intensity. We also observed a dramatic change in the Raman spectra starting at 7 nm thickness. The possible reason is that the spin ordering is changed along the sample thinning. The spin-lattice coupling is noticeable in CrSiTe<sub>3</sub> and different spin states could lead to different lattice constants,<sup>8</sup> thus inducing different phonon frequencies. However, further studies on spin are needed.

We have fabricated 2D CrSiTe<sub>3</sub> field-effect transistor (FET) devices using standard electron-beam lithography. Fig. 4(a) depicts a schematic diagram of the 2D CrSiTe<sub>3</sub> FET device on a Si/SiO<sub>2</sub> substrate with source/drain electrodes. The optical micrograph also demonstrates a clear image of the 2D CrSiTe<sub>3</sub> FET device shown in Fig. 4(b). Although we are able to thin CrSiTe<sub>3</sub> crystals down to a single layer, successful devices with good electrical contacts can be prepared only on flakes with thickness  $\geq 7$  nm. Based on the measurement of output curves shown in Fig. 4(c) in a back-gating configuration, these CrSiTe<sub>3</sub> FET devices display p-type semiconductor characteristics. The linear output curves indicate nearly Ohmic contacts at 295 K and 6 K. Fig. 4(d) shows the  $I_{ds}$ - $V_{bg}$  transfer curves measured on a 7 nm thick CrSiTe<sub>3</sub> device at different temperatures down to 6 K with  $V_{ds} = 1$  V. The inset in Fig. 4(d) the mobility increased with temperature, demonstrating the same trend as found in single layer MoS<sub>2</sub> for the same gating configuration.<sup>43</sup> The mobility ( $\sim 0.01$  cm<sup>2</sup> V<sup>-1</sup> s<sup>-1</sup> at  $T = 295$  K) was calculated using the eqn  $\mu = \frac{1}{C_{ox}} \left( \frac{L}{WV_{ds}} \right) \left( \frac{dI}{dV_{bg}} \right)$  extracted from the linear region of the transport curves  $I_{ds}$ - $V_{bg}$ , where  $L$  is the channel length,  $W$  is the channel width,  $V_{ds} = 1$  V and  $C_{ox} = 1.2 \times 10^{-8}$  F cm<sup>-2</sup> is

the capacitance between the channel and the back gate per unit area ( $C_{ox} = \epsilon_0 \epsilon_r / d_{ox}$ ,  $\epsilon_0 = 8.85 \times 10^{-12}$  F m<sup>-1</sup>,  $\epsilon_r = 3.9$  and  $d_{ox} = 290$  nm).

The electronic band structure of monolayer CrSiTe<sub>3</sub> was calculated from first-principles calculations using DFT. Fig. 5(a) shows the spin-polarized electronic band structures of monolayer CrSiTe<sub>3</sub>, confirming an indirect bandgap. The bandgaps of FM ordering as a function of  $U_{eff}$  are presented in Fig. S1(c) (ESI<sup>†</sup>). The gap sizes for spin-up and spin-down states are 0.57 eV and 0.65 eV, respectively. For bulk CrSiTe<sub>3</sub>, using the same  $U_{eff}$  the calculated spin-up and spin-down bandgaps are 0.39 eV and 0.65 eV,<sup>8</sup> respectively. The enhanced spin-up bandgap of monolayer CrSiTe<sub>3</sub> compared to that of the bulk is due to quantum confinement, which is an intrinsic property at low dimensionality and similar to other 2D semiconductors.<sup>44,45</sup> Furthermore, Fig. 5(b) shows the density of states of monolayer CrSiTe<sub>3</sub>, which illustrates that the Cr d and Te p orbitals are involved in superexchange interactions between the spins of neighboring Cr<sup>3+</sup> ions.

Table 1 provides a comparison between FM and AFM structure, magnetic moment and formation energy as determined by first-principles calculations for monolayer CrSiTe<sub>3</sub>. As can be seen, the lattice constants of monolayer CrSiTe<sub>3</sub> with both FM (6.69 Å) and AFM (6.66 Å) orderings are similar, as are their magnetic moments. The calculated magnetic moments are 3.0  $\mu_B$  for both magnetic orderings. This value is the same as the spin magnetic moment of an isolated Cr<sup>3+</sup> ion, implying that the orbital magnetic moments are largely quenched in monolayer CrSiTe<sub>3</sub>. Indeed, turning on spin-orbit coupling (SOC) in the calculation yields a similar total magnetic moment, which indicates a weak SOC. The ground state energy of monolayer CrSiTe<sub>3</sub> was calculated for both FM and AFM orderings.

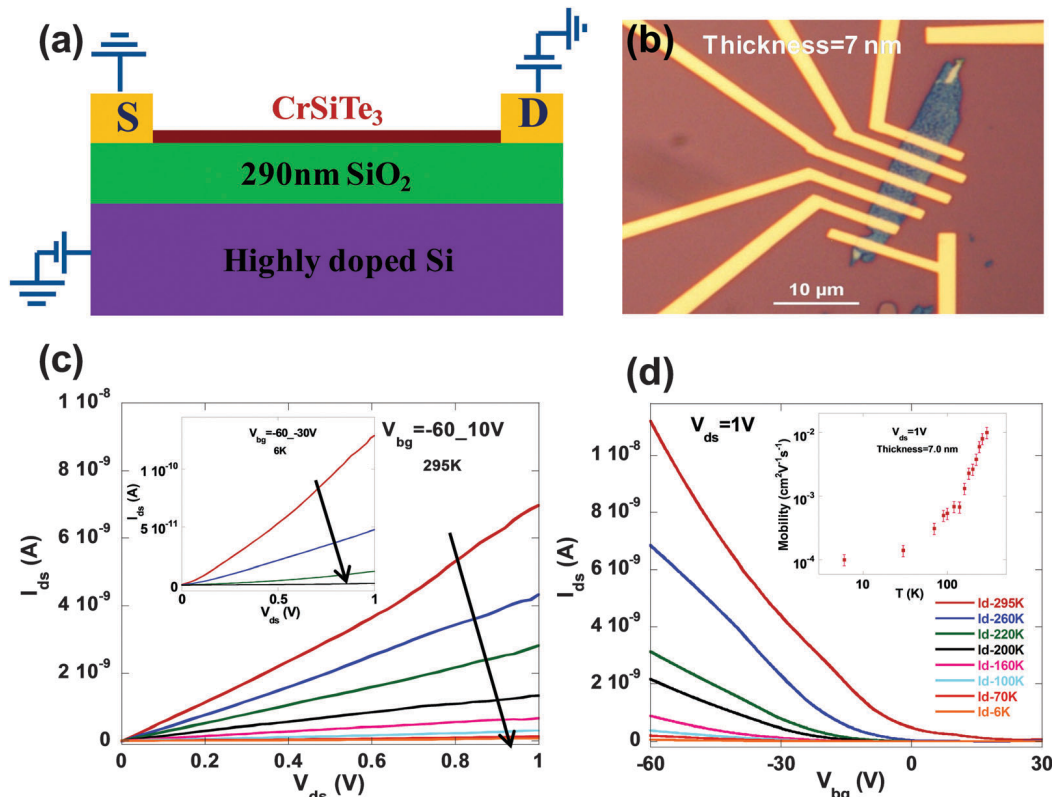


Fig. 4 Schematic diagram, optical micrograph and characteristics of a CrSiTe<sub>3</sub> FET device. (a) Schematic of a CrSiTe<sub>3</sub> FET device on Si/SiO<sub>2</sub> substrate showing the source/drain electrodes. (b) OM image showing top view of CrSiTe<sub>3</sub> FET devices with electrodes. (c)  $I_{ds}$ - $V_{ds}$  output curves are nearly linear suggesting the device contacts are essentially Ohmic at 295 K. Inset is the  $I_{ds}$ - $V_{ds}$  curves at 6 K. (d) The transfer curve shows p-type semiconductor behavior down to 6 K. The mobility as a function of temperature for a 7.0 nm thick CrSiTe<sub>3</sub> FET device in the inset, indicating the mobility decreases as decreasing temperature.

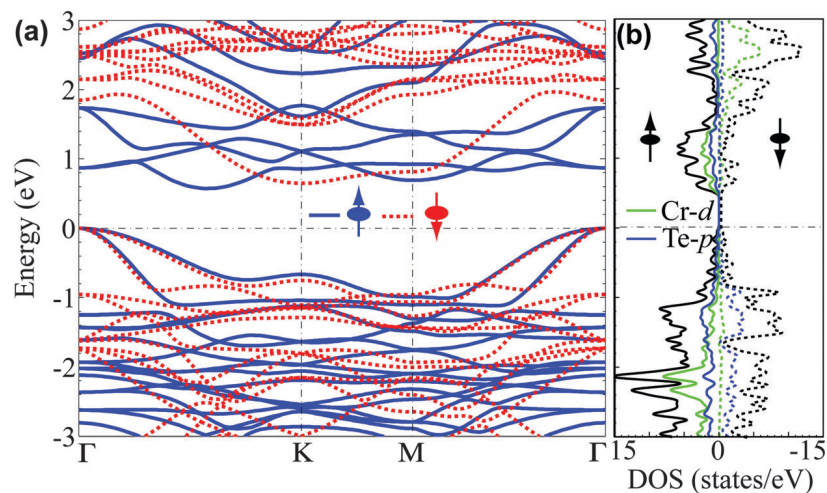


Fig. 5 Electronic band structure obtained from first-principles calculations using density-functional theory (DFT). (a) The electronic band structures of spin-up and spin-down is denoted as blue and red. (b) Spin density of states show the bandgap of monolayer of CrSiTe<sub>3</sub> with the gap size 0.57 eV and 0.65 eV for spin up and spin down, respectively.

The possible antiferromagnetic spin textures, Néel, stripy, and zigzag configurations, have been considered and computed (see Fig. S4, ESI<sup>†</sup>). Furthermore, we calculated the first, second, and third nearest-neighboring exchange constants with the computation details described in the ESI<sup>†</sup> and determined  $J_1$ ,

$J_2$ , and  $J_3$  as  $-2.39$  meV,  $0.00$  meV, and  $+0.18$  meV, respectively. This suggests that the dominant exchange coupling comes from the first nearest-neighboring Cr-Cr pair interactions. Therefore, the energy of a FM monolayer CrSiTe<sub>3</sub> is smaller than the AFM one, showing that the ground-state monolayer

**Table 1** Comparison between ferromagnetic (FM) and antiferromagnetic (AFM) structure (lattice constant  $a_0$ ), magnetic moment  $\mu_B$ , and formation energy  $E_f$  for monolayer CrSiTe<sub>3</sub>

	$a_0$ (Å)	$\mu$ ( $\mu_B$ )	$E_f$
FM	6.69	3.0	43.7
AFM	6.66	3.0	48.7

CrSiTe<sub>3</sub> exhibits ferromagnetic ordering. In addition, we carried out similar calculations of exchange coupling constants for p-type doped single-layer CrSiTe<sub>3</sub> by using a  $2 \times 2$  supercell model with 0.155 electrons removed from the same supercell of pristine single-layer CrSiTe<sub>3</sub> with 288 electrons. This is equivalent to p-type doping with a very high hole concentration of  $10^{13}$  cm<sup>-2</sup>. From Fig. S4(f) (ESI<sup>†</sup>), we can see that the FM structure is still the ground state. Following the same procedure, we obtain the exchange coupling parameters of  $-2.39$  meV,  $0.02$  meV, and  $+0.18$  meV, which are nearly identical to those in the undoped case. This suggests that p-type doping almost has no effect on the Curie temperature.

Another important characteristic of the 2D CrSiTe<sub>3</sub> material is ferromagnetism perseverance in low dimensionality with changing Curie temperature  $T_c$ . The  $T_c$  change has been reported in other multilayered systems from 3D to 2D.<sup>21–22,46,47</sup> From our theoretical calculations using a 2D Ising model,  $T_c$  can reach values up to  $\sim 80$  K for monolayer CrSiTe<sub>3</sub> with a magnetic moment of  $3 \mu_B$  as shown in Fig. 6(a). The inset of Fig. 6(a) shows the susceptibility as a function of temperature for monolayer CrSiTe<sub>3</sub>. The higher  $T_c$  in monolayer CrSiTe<sub>3</sub> can be understood as possibly resulting from the competition between interlayer and intralayer exchange interactions compared with bulk. The exchange coupling interaction becomes dominated by intralayer Cr–Cr superexchange mediated by Te ions as one proceeds toward a monolayer of CrSiTe<sub>3</sub>, which gives higher in-plane interaction energy associated with higher  $T_c$ . Theoretical calculations also indicate higher energy for exchange coupling resulting from intralayer *versus* interlayer interactions. The resistivity

measured for a 7 nm thick 2D CrSiTe<sub>3</sub> device shown in Fig. 6(b) is seen to increase exponentially with decreasing temperature in the high temperature regime, but then clearly deviates from this behavior starting at 140 K. We found that the resistivities measured between 100–140 K significantly deviated from the average value below 100 K (shown by the dashed line in Fig. 6(b)) which we attribute to instrumental resolution. Very similar resistivity *versus* temperature was measured for devices with thicknesses of 8.5 nm and 20 nm (shown in Fig. S3, ESI<sup>†</sup>). Altogether, the devices showed transitions from the expected exponential increase in resistivity with decreasing temperature, with clear and measurable deviations from this behavior at temperatures ranging between 80–120 K (shown by arrows in Fig. S3, ESI<sup>†</sup>). Some published results on metal thin film systems have shown that the critical temperature of a FM to AFM phase transition is accompanied by an abrupt change in resistivity at that temperature due to scattering caused by a change of magnetic moments.<sup>48,49</sup> In our data, the abrupt transition temperature for the resistivity is generally found to decrease with decreasing number of layers, which we believe is likely due to changes in magnetic ordering with reducing dimensionality. This explanation relies upon the plausible existence of AFM or FM ordering in 2D magnetic semiconductors down to very thin layers. However, absolute proof of the magnetization of monolayer CrSiTe<sub>3</sub> by SQUID measurements is currently extremely complicated due to a very weak signal and the difficulty in preparing uniform 2D flakes using mechanical exfoliation. Such measurements will be the subject of future studies.

## Conclusions

In conclusion, monolayer and few-layer samples of 2D FM CrSiTe<sub>3</sub> crystals were isolated after exfoliation and characterized by Raman spectroscopy, allowing the identification of the Raman-active modes predicted from the calculated phonon spectra and confirming the theoretical predictions that monolayer CrSiTe<sub>3</sub>

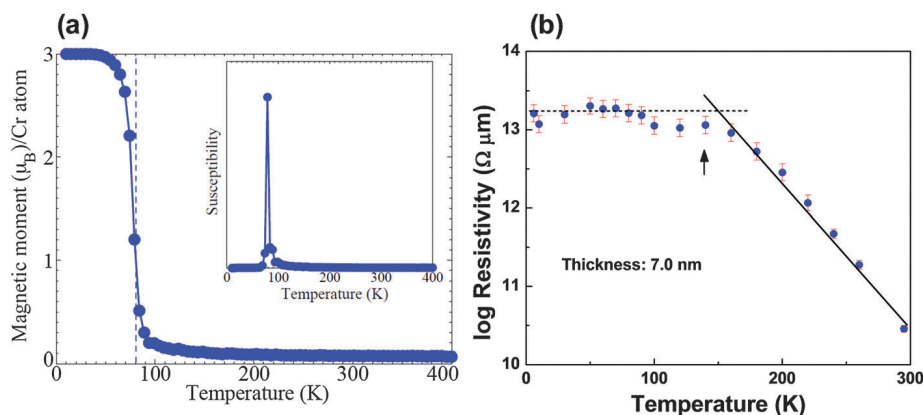


**Fig. 6** (a) The calculated transition temperature ( $T_c$ ) with magnetic moment  $3 \mu_B$  for monolayer CrSiTe<sub>3</sub> using 2D Ising model Monte Carlo simulations with the exchange parameter from the LDA+U calculations. Inset shows the susceptibility as function of temperature for monolayer CrSiTe<sub>3</sub>. (b) The plot of logarithmic resistivity vs. temperature for a CrSiTe<sub>3</sub> flake of 7 nm thickness, exhibiting an expected increase in resistivity with decreasing temperature in the high temperature regime, but with a clear deviation from this behavior beginning  $\sim 140$  K, indicating a possible FM–AFM phase transition at that temperature. The dashed line indicates the average resistivity for measurements  $T < 100$  K.

is dynamically stable. The exfoliated few-layer samples retained the p-type semiconductor characteristics of bulk CrSiTe<sub>3</sub>, as characterized by FET devices fabricated from the lithographically-addressed 2D crystals. Ising model calculations predicted an elevated Curie temperature ( $T_c \sim 80$  K) for the magnetic ordering of monolayer 2D CrSiTe<sub>3</sub> crystals, significantly increased from the bulk ( $T_c \sim 33$  K). Consistent with these predictions, temperature-dependent resistivity measurements for the few-layer 2D CrSiTe<sub>3</sub> FET devices indicate a clear change in resistivity at elevated temperatures of 80–120 K. These results indicate that ferromagnetic mono- and few-layer 2D CrSiTe<sub>3</sub> crystals are promising ultrathin nanomaterials for potential applications in spintronics.

## Acknowledgements

Device fabrication was supported by the Laboratory Directed Research and Development program (LDRD) project and Raman measurements were conducted at Center for Nanophase Materials Sciences, which is sponsored at Oak Ridge National Laboratory by the Scientific User Facilities Division, Office of Basic Energy Sciences, U.S. Department of Energy. DGM and JQY acknowledge support from the National Science Foundation under Grant No. NSF DMR-1410428. TZW acknowledge support from the US Department of Energy (DOE), Office of Basic Energy Sciences (BES), Materials Sciences and Engineering Division for PPMS measurements. HZ, PG, PRCK acknowledge support from LDRD project for theoretical calculations. LL was supported as a Eugene P. Wigner Fellow at Oak Ridge National Laboratory.

## Notes and references

- 1 Q. H. Wang, K. Kalantar-Zadeh, A. Kis, J. N. Coleman and M. S. Strano, *Nat. Nanotechnol.*, 2012, **7**, 699–712.
- 2 A. K. Geim and I. V. Grigorieva, *Nature*, 2013, **499**, 419–425.
- 3 V. Nicolosi, M. Chhowalla, M. G. Kanatzidis, M. S. Strano and J. N. Coleman, *Science*, 2013, **340**, 1226419.
- 4 S. Lebegue, T. Björkman, M. Klintonberg, R. Nieminen and O. Eriksson, *Phys. Rev. X*, 2013, **3**, 031002.
- 5 B. Sachs, T. O. Wehling, K. S. Novoselov, A. I. Lichtenstein and M. I. Katsnelson, *Phys. Rev. B: Condens. Matter Mater. Phys.*, 2013, **88**, 201402.
- 6 N. Sivadas, M. W. Daniels, R. H. Swendsen, S. Okamoto and D. Xiao, *Phys. Rev. B: Condens. Matter Mater. Phys.*, 2015, **91**, 235425.
- 7 V. Cartheaux, G. Ouvrard, J. C. Grenier and Y. Lalignant, *J. Magn. Magn. Mater.*, 1991, **94**, 127–133.
- 8 L. D. Casto, A. J. Clune, M. O. Yokosuk, J. L. Musfeldt, T. J. Williams, H. L. Zhuang, M.-W. Lin, K. Xiao, R. G. Hennig, B. C. Sales, J.-Q. Yan and D. Mandrus, *APL Mater.*, 2015, **3**, 041515.
- 9 H. Kabbour, R. David, A. Pautrat, H.-J. Koo, M.-H. Whangbo, G. André and O. Mentré, *Angew. Chem., Int. Ed.*, 2012, **51**, 11745–11749.
- 10 M. A. McGuire, H. Dixit, V. R. Cooper and B. C. Sales, *Chem. Mater.*, 2015, **27**, 612–620.
- 11 I. Yamada, *J. Phys. Soc. Jpn.*, 1972, **33**, 979–988.
- 12 S. Tongay, S. S. Varnoosfaderani, B. R. Appleton, J. Wu and A. F. Hebard, *Appl. Phys. Lett.*, 2012, **101**, 123105.
- 13 Z. Zhang, X. Zou, V. H. Crespi and B. I. Yakobson, *ACS Nano*, 2013, **7**, 10475–10481.
- 14 H. Pan and Y.-W. Zhang, *J. Phys. Chem. C*, 2012, **116**, 11752–11757.
- 15 S. Yang, C. Wang, H. Sahin, H. Chen, Y. Li, S.-S. Li, A. Suslu, F. M. Peeters, Q. Liu, J. Li and S. Tongay, *Nano Lett.*, 2015, **15**, 1660–1666.
- 16 M. N. Ali, J. Xiong, S. Flynn, J. Tao, Q. D. Gibson, L. M. Schoop, T. Liang, N. Haldolaarachchige, M. Hirschberger, N. P. Ong and R. J. Cava, *Nature*, 2014, **514**, 205–208.
- 17 L. Cai, J. He, Q. Liu, T. Yao, L. Chen, W. Yan, F. Hu, Y. Jiang, Y. Zhao, T. Hu, Z. Sun and S. Wei, *J. Am. Chem. Soc.*, 2015, **137**, 2622–2627.
- 18 N. Mermin and H. Wagner, *Phys. Rev. Lett.*, 1966, **17**, 1133–1136.
- 19 P. Bruno, *Phys. Rev. Lett.*, 2001, **87**, 137203.
- 20 M. Pomerantz, *Surf. Sci.*, 1984, **142**, 556–570.
- 21 Y. Li and K. Baberschke, *Phys. Rev. Lett.*, 1992, **68**, 1208–1211.
- 22 M. A. Medvedeva and P. V. Prudnikov, *J. Phys.: Conf. Ser.*, 2014, **510**, 012024.
- 23 M. Osada, Y. Ebina, K. Fukuda, K. Ono, K. Takada, K. Yamaura, E. Takayama-Muromachi and T. Sasaki, *Phys. Rev. B: Condens. Matter Mater. Phys.*, 2006, **73**, 153301.
- 24 X. Zhang, J. Zhang, J. Zhao, B. Pan, M. Kong, J. Chen and Y. Xie, *J. Am. Chem. Soc.*, 2012, **134**, 11908–11911.
- 25 T. Taniguchi, K. Yamaguchi, A. Shigeta, Y. Matsuda, S. Hayami, T. Shimizu, T. Matsui, T. Yamazaki, A. Funatstu, Y. Makinose, N. Matsushita, M. Koinuma and Y. Matsumoto, *Adv. Funct. Mater.*, 2013, **23**, 3140–3145.
- 26 M. Osada, S. Yoguchi, M. Itose, B.-W. Li, Y. Ebina, K. Fukuda, Y. Kotani, K. Ono, S. Ueda and T. Sasaki, *Nanoscale*, 2014, **6**, 14227–14236.
- 27 G. Ouvrard, E. Sandre and R. Brec, *J. Solid State Chem.*, 1988, **73**, 27–32.
- 28 V. Cartheaux, F. Moussa and M. Spiesser, *EPL*, 1995, **29**, 251–256.
- 29 T. J. Williams, A. A. Aczel, M. D. Lumsden, S. E. Nagler, M. B. Stone, J.-Q. Yan and D. Mandrus, 2015, *arXiv*: 1503.08199v1.
- 30 X. Li and J. Yang, *J. Mater. Chem. C*, 2014, **2**, 7071–7076.
- 31 X. Chen, J. Qi and D. Shi, *Phys. Lett. A*, 2015, **379**, 60–63.
- 32 H. L. Zhuang, Y. Xie, P. R. C. Kent and P. Ganesh, *Phys. Rev. B: Condens. Matter Mater. Phys.*, 2015, **92**, 035407.
- 33 X. Wang, Y. Gong, G. Shi, W. L. Chow, K. Keyshar, G. Ye, R. Vajtai, J. Lou, Z. Liu, E. Ringe, B. K. Tay and P. M. Ajayan, *ACS Nano*, 2014, **8**, 5125–5131.
- 34 X. Li, M.-W. Lin, A. A. Puzdov, J. C. Idrobo, C. Ma, M. Chi, M. Yoon, C. M. Rouleau, I. I. Kravchenko, D. B. Geohegan and K. Xiao, *Sci. Rep.*, 2014, **4**, 5497.
- 35 K. S. Novoselov, A. K. Geim, S. V. Morozov, D. Jiang, Y. Zhang, S. V. Dubonos, I. V. Grigorieva and A. A. Firsov, *Science*, 2004, **306**, 666–669.

- 36 X. Li, X. Wu and J. Yang, *J. Am. Chem. Soc.*, 2014, **136**, 11065–11069.
- 37 G. Kresse and J. Furthmüller, *Comput. Mater. Sci.*, 1996, **6**, 15–50.
- 38 G. Kresse and D. Joubert, *Phys. Rev. B: Condens. Matter Mater. Phys.*, 1999, **59**, 1758–1775.
- 39 A. I. Liechtenstein, V. I. Anisimov and J. Zaanen, *Phys. Rev. B: Condens. Matter Mater. Phys.*, 1995, **52**, R5467–R5470.
- 40 L. Liang and V. Meunier, *Nanoscale*, 2014, **6**, 5394–5401.
- 41 K. Parlinski, Z. Q. Li and Y. Kawazoe, *Phys. Rev. Lett.*, 1997, **78**, 4063–4066.
- 42 K. Parlinski, *Computer Code PHONON*, Krakow, Poland, 2010.
- 43 B. Radisavljevic and A. Kis, *Nat. Mater.*, 2013, **12**, 815–820.
- 44 G. W. Mudd, S. A. Svatek, T. Ren, A. Patané, O. Makarovskiy, L. Eaves, P. H. Beton, Z. D. Kovalyuk, G. V. Lashkarev, Z. R. Kudrynskiy and A. I. Dmitriev, *Adv. Mater.*, 2013, **25**, 5714–5718.
- 45 Y. Yoon, K. Ganapathi and S. Salahuddin, *Nano Lett.*, 2011, **11**, 3768–3773.
- 46 A. Du and G. Wei, *Aust. J. Phys.*, 1993, **46**, 571–582.
- 47 L. Capriotti, R. Vaia, A. Cuccoli and V. Tognetti, *Phys. Rev. B: Condens. Matter Mater. Phys.*, 1998, **58**, 273–281.
- 48 J. S. Kouvel and C. C. Hartelius, *J. Appl. Phys.*, 1962, **33**, 1343–1344.
- 49 M. A. D. Vries, M. Loving, A. P. Mihai, L. H. Lewis, D. Heiman and C. H. Marrows, *New J. Phys.*, 2013, **15**, 013008.